Available online at www.sciencedirect.com
SCIENCE DIRECT®
International Journal of Solids and Structures 42 (2005) 1649–1667
INTERNATIONAL JOURNAL OF SOLIDS and STRUCTURES
www.elsevier.com/locate/ijsolstr

A shear-lag model for carbon nanotube-reinforced polymer composites

X.-L. Gao [a,*], K. Li [b]

[a] Department of Mechanical Engineering, Texas A&M University, 3123 TAMU, College Station, TX 77843-3123, USA
[b] Department of Mechanical Engineering—Engineering Mechanics, Michigan Technological University, 1400 Townsend Drive, Houghton, MI 49931-1295, USA

Received 2 February 2004; received in revised form 22 August 2004
Available online 13 October 2004

Abstract

A shear-lag model is developed for carbon nanotube-reinforced polymer composites using a multiscale approach. The main morphological features of the nanocomposites are captured by utilizing a composite cylinder embedded with a capped nanotube as the representative volume element. The molecular structural mechanics is employed to determine the effective Young's modulus of the capped carbon nanotube based on its atomistic structure. The capped nanotube is equivalently represented by an effective (solid) fiber having the same diameter and length but different Young's modulus, which is determined from that of the nanotube under an isostrain condition. The shear-lag analysis is performed in the context of linear elasticity for axisymmetric problems, and the resulting formulas are derived in closed forms. To demonstrate applications of the newly developed model, parametric studies of sample cases are conducted. The numerical results reveal that the nanotube aspect ratio is a critical controlling parameter for nanotube-reinforced composites. The predictions by the current analytical model compare favorably with the existing computational and experimental data.
© 2004 Elsevier Ltd. All rights reserved.

Keywords: Carbon nanotube; Nanocomposite; Shear-lag model; Interfacial stress transfer; Multiscale modeling; Polymer composite; Elasticity; Molecular structural mechanics

* Corresponding author. Tel.: +1 979 845 4835; fax: +1 979 845 3081.
E-mail address: xlgao@tamu.edu (X.-L. Gao).

0020-7683/$ - see front matter © 2004 Elsevier Ltd. All rights reserved.
doi:10.1016/j.ijsolstr.2004.08.020

1. Introduction

Carbon nanotubes have been identified as promising reinforcing materials for high-performance nanocomposites (e.g., Ajayan et al., 2000; Thostenson et al., 2001; Maruyama and Alam, 2002). To this end, however, many critical issues are yet to be resolved, one of which is the lack of accurate understanding of mechanisms of load transfer from the matrix to the nanotubes (e.g., Wagner, 2002).

Efforts have been made to assess the ability of stress transfer through the nanotube–matrix interface (e.g., Wagner et al., 1998; Schadler et al., 1998; Qian et al., 2000; Lordi and Yao, 2000; Liao and Li, 2001; Frankland et al., 2002, 2003; Frankland and Harik, 2003; Barber et al., 2003). These studies, being based on experimental measurements or molecular dynamics simulations, tend to be expensive and configuration/material specific. The use of continuum-based models can mitigate these difficulties (e.g., Odegard et al., 2002; Zhang et al., 2002; Li and Chou, 2003a; Gao and Li, 2003; Pantano et al., 2004) and is, therefore, very desirable. The interfacial shear strength in polymer composites reinforced by single-walled carbon nanotubes has recently been estimated by Wagner (2002) using a modified Kelly–Tyson approach that is continuum-based and assumes uniform interfacial shear and axial normal stresses. More recently, a continuum-based computational model for interfacial stress transfer in nanotube-reinforced polymer composites has been developed by Li and Chou (2003b), which employs the molecular structural mechanics proposed by the same authors (Li and Chou, 2003a) to characterize the nanotube and the finite element method to model the polymer matrix. This study sheds new light on the understanding of the load transfer across the nanotube–matrix interface and provides needed guidance for the development of analytical models.

The stress transfer problem for traditional fiber-reinforced composites has been extensively studied. The shear-lag model originally proposed by Cox (1952) provides a good estimate of the stresses in the fiber transferred from the matrix through the interface. However, this analytical model cannot be directly applied to characterize nanotube-reinforced composites, since it considers the load transfer across the curved interface only and regards the fiber ends as traction-free. In addition, some important morphological features of nanotube-reinforced composites are not incorporated in existing shear-lag models. It is known that the efficiency of the nanotube reinforcement depends sensitively on the morphology (including diameter, wall thickness and chirality) and distribution of the nanotubes (e.g., Thostenson and Chou, 2003). This necessitates the incorporation of atomistic structures of carbon nanotubes in developing continuum-based analytical models of shear-lag type for nanotube-reinforced composites.

The objective of the current study is to develop such a shear-lag model using a representative volume element (RVE) of a concentric composite cylinder embedded with a capped carbon nanotube. The rest of the paper is organized as follows. In Section 2, the molecular structural mechanics of Li and Chou (2003a), together with the matrix method for spatial frames (e.g., Li et al., 2003), is first employed to predict the effective Young's modulus of the nanotube. The capped nanotube is then replaced by an effective (solid) fiber, whose length and diameter are kept to be the same as those of the nanotube to preserve the essential morphological features of the nanocomposite. The Young's modulus of the effective fiber is subsequently determined under an isostrain condition. This is followed by the development of the shear-lag model in Section 3 using the cylindrical RVE. In Section 4, sample numerical results are presented to demonstrate applications of the newly developed model. The paper concludes with a summary in the fifth and last section.

2. Capped nanotube as an effective fiber

After numerous efforts by many researchers, it has become possible to fabricate nanotube-reinforced polymer composites with well-dispersed and well-aligned nanotubes (e.g., Haggenmueller et al., 2000; Bower et al., 2000; Thostenson and Chou, 2002; Cooper et al., 2002). As a first step toward simulating such

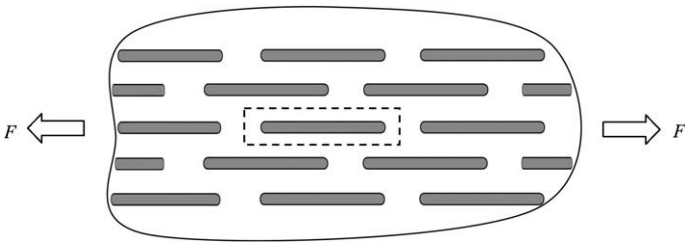

Fig. 1. Model nanocomposite.

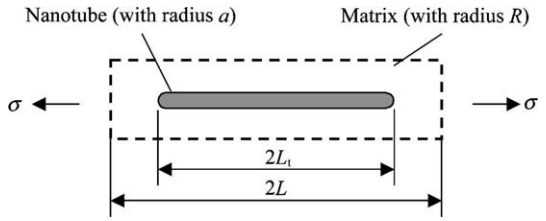

Fig. 2. RVE of the model nanocomposite.

composites using continuum-based analytical approaches, consider a model composite reinforced by uniformly distributed and perfectly aligned identical nanotubes, as shown in Fig. 1. The representative volume element (RVE) of the composite is sketched in Fig. 2, where the nanotube with two end caps is regarded as perfectly bonded to the matrix and located at the center of the RVE, with both the matrix and the nanotube phases being isotropic. The cylindrical RVE of this type has been adopted earlier by Li and Chou (2003b), but in their model the nanotube is assumed to be uncapped.

The shear-lag model to be developed will be based on the RVE shown in Fig. 2. The development of this continuum model requires that the structurally discrete nanotube be replaced by a continuum phase. To this end, the capped nanotube embedded in the matrix will first be represented as an effective (solid) fiber, whose Young's modulus is determinable from that of the nanotube. The latter will be predicted using the molecular structural mechanics approach advanced by Li and Chou (2003a), which incorporates the atomistic structure of the nanotube and is based on the equivalence of the strain energy and the molecular potential energy.

A fairly large number of studies have been conducted to predict elastic properties of carbon nanotubes without caps. In contrast, very limited attention has been paid to capped nanotubes, although numerous experiments indicate that carbon nanotubes are usually closed at both ends (Harris, 1999). This is partially due to the complexity associated with nanotube capping. For example, it has been shown by Fujita et al. (1992) that only nanotubes that are larger than the archetypal $(5,5)$ and $(9,0)$ tubes are capable of being capped, and that the number of possible caps grows significantly with the increase of the nanotube diameter.

The chirality and diameter of a nanotube can be uniquely determined by the roll-up (chiral) vector (m,n) (e.g., Saito et al., 1993; Thostenson et al., 2001), where m and n are non-negative integers representing the number of steps along the zigzag carbon bonds of the hexagonal lattice. A carbon nanotube designated by (m,n) is generally chiral, unless $m = n$ or $n = 0$ to become an armchair or zigzag nanotube.

A capped carbon nanotube (graphene tubule) may be formed by adding hexagons between two hemispheres cut from an icosahedral fullerene, which corresponds to a spherical Goldberg polyhedron

(Fujita et al., 1992). Through defining a chiral vector (m_f, n_f) for specifying an icosahedral fullerene, where m_f and n_f are non-negative integers, the total number of atoms for the fullerene is given by $20(m_f^2 + m_f n_f + n_f^2)$. When $m_f = n_f$ or m_f $n_f = 0$, two groups of fullerenes with the icosahedral symmetry (I_h) are obtained, i.e., the series of $C_{60}, C_{240}, \ldots, C_{60n_f^2}$ and the series of $C_{20}, C_{80}, \ldots, C_{20n_f^2}$ (where C_{20} is unable to nucleate a tubule). In other cases, the fullerenes have the I symmetry (which is a subset of I_h involving no inversion operation). The carbon nanotube that nucleates from two halves of a fullerene can be designated by $(5m_f, 5n_f)$. Another group of zigzag nanotubes, i.e., $(9,0),(18,0),\ldots,(9n_f,0)$, can be capped by hemispheres cut from icosahedral fullerenes $C_{60}, C_{240}, \ldots, C_{60n_f^2}$, which correspond to the chiral vectors $(1,1),(2,2),\ldots,(n_f,n_f)$, in a direction perpendicular to one of the three-fold axes (Saito et al., 1992). The caps for armchair nanotubes $(5,5),(10,10),\ldots,(5n_f,5n_f)$ are obtained by bisecting the same group of fullerenes in a direction perpendicular to one of the five-fold axes (Saito et al., 1992). Halves of fullerene C_{60} could cap armchair nanotube $(5,5)$ or zigzag nanotube $(9,0)$, the two smallest carbon nanotubes that can be capped.

Using molecular dynamics (MD) simulations, Yao and Lordi (1998) modeled capped single-walled and multi-walled carbon nanotubes with armchair chirality. By assuming that nanotubes are made of a continuum and employing Harrison's tight-binding model, Glukhova et al. (2003) estimated the average Young's modulus of capped zigzag carbon nanotubes. However, molecular dynamics and tight-binding methods typically involve extensive computations and, therefore, are limited to modeling systems embracing a small number of atoms and undergoing a short period of time. In contrast, the molecular structural mechanics (MSM) approach developed by Li and Chou (2003a) is computationally efficient. By viewing a nanotube as a spatial frame, the covalent bonds between carbon atoms as equivalent structural beams and individual atoms as joints, they showed that a linkage between structural mechanics and molecular mechanics can be established. Then, the cross-sectional parameters of the equivalent beams (with circular cross-sections), which are required to form the elemental stiffness matrices for structural mechanics analysis based on the matrix method for spatial frames, can be determined from the equivalence of the corresponding steric potential energies of atomic bonds and elemental strain energies of structural beams. Therefore, the MSM approach of Li and Chou is employed here to calculate the effective Young's modulus of each capped single-walled carbon nanotube. The computer program developed by Li et al. (2003) for the matrix method in a more general context is used in the calculation to determine the displacements at unrestrained joints.

Three capped armchair nanotubes, i.e., $(5,5)$, $(10,10)$ and $(15,15)$, and five capped zigzag nanotubes, i.e., $(9,0)$, $(10,0)$, $(15,0)$, $(20,0)$ and $(25,0)$, with different values of axial length, are considered in the current study. The force field constants are taken to be $k_r/2 = 469\,\text{kcal}\cdot\text{mol}^{-1}\,\text{Å}^{-2}$, $k_\theta/2 = 63\,\text{kcal}\cdot\text{mol}^{-1}\,\text{rad}^{-2}$ and $k_\tau/2 = 20\,\text{kcal}\cdot\text{mol}^{-1}\,\text{rad}^{-2}$, and the initial carbon–carbon bond length to be 0.1421 nm, all as initially used in Li and Chou (2003a). Due to symmetry, only half of a nanotube needs to be modeled, as shown in Fig. 3. Also, the open end may be reviewed as a fixed support with no displacement or rotation. By applying a concentrated axial force F to each of the joints on the cap, the Young's modulus of the nanotube, E_t, can be determined as

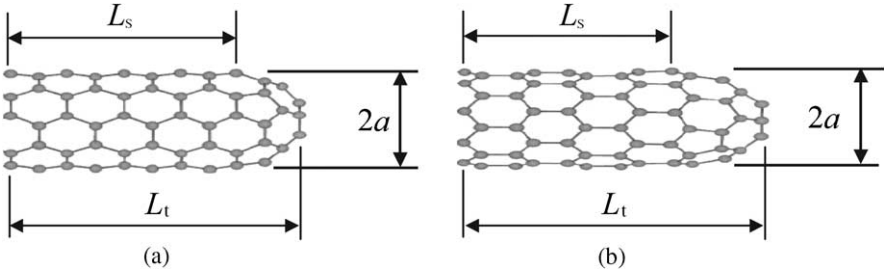

Fig. 3. Half of a capped nanotube: (a) armchair (b) zigzag.

$$E_t = \frac{\beta F L_s}{2\pi a t \Delta L_s}, \tag{1}$$

where a is the outer radius of the nanotube, t is the tube wall thickness [taken to be 0.34 nm, the interlayer spacing of graphite sheets, as was done in Li and Chou (2003a)], L_s is the length from the open end to the tube-cap intersection, ΔL_s is the axial displacement of each joint at the intersection that is obtained using the matrix method mentioned above, and β is the total number of joints on the cap including those at the intersection. With the involvement of t in Eq. (1), the degree of hollowness of the nanotube is automatically accounted for in determining E_t.

The predicted values of Young's modulus (E_t) versus the aspect ratio (L_t/a) for uncapped nanotubes are presented in Figs. 4 and 5. From these two figures, one can observe that the trend of E_t varying with L_t/a is similar for both the armchair and zigzag nanotubes. It is also seen that E_t increases rapidly with L_t/a when $L_t/a < 10$, beyond which E_t remains almost constant. A further inspection of these two figures indicates that E_t increases monotonically with the nanotube diameter.

For capped nanotubes, as shown in Figs. 6 and 7, the trend of E_t varying with L_t/a is similar to that of the uncapped nanotubes. The aspect ratio L_t/a has little influence on E_t for armchair nanotubes (see Fig. 6).

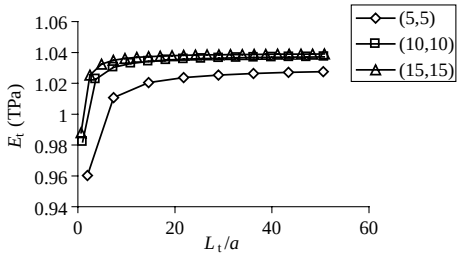

Fig. 4. Young's modulus of uncapped nanotubes (armchair).

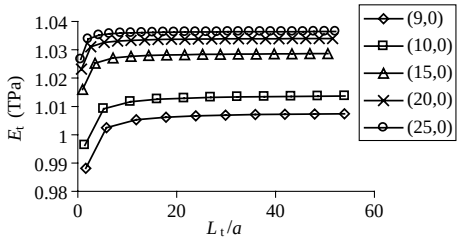

Fig. 5. Young's modulus of uncapped nanotubes (zigzag).

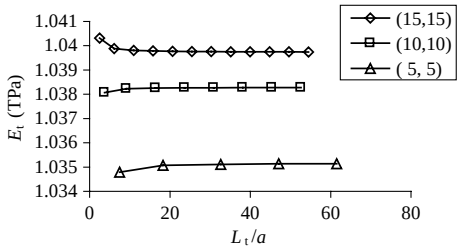

Fig. 6. Young's modulus of capped nanotubes (armchair).

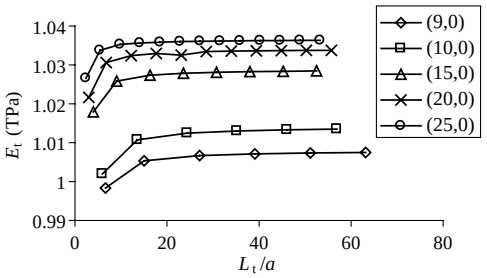

Fig. 7. Young's modulus of capped nanotubes (zigzag).

For zigzag nanotubes, E_t increases with L_t/a when L_t/a is small, but remains almost constant when $L_t/a > 20$ (see Fig. 7). The increasing rate (i.e., slope) here appears to be smaller than that of the corresponding uncapped zigzag nanotube (see Figs. 5 and 7).

When L_t/a is fixed, the effect of the nanotube diameter $2a$ on E_t is shown in Fig. 8. It is seen that the armchair nanotubes are stiffer than the zigzag nanotubes and the difference in Young's modulus is reduced as $2a$ increases, which agrees with the earlier findings by Popov et al. (2000) based on a lattice dynamics model and Chang and Gao (2003) using molecular mechanics. From Fig. 8, one can also observe that for armchair nanotubes the capped ones are slightly stiffer than the uncapped ones when $2a < 1.3$ nm, and that the stiffness difference decreases as $2a$ increases. For zigzag nanotubes, the differences in Young's modulus of the capped and uncapped ones are negligibly small. These observations indicate that the effect of capping is insignificant for sufficiently long and large nanotubes.

With the effective Young's modulus of the nanotube determined based on its atomistic structure, the nanotube embedded in the matrix can then be replaced by an effective (solid) fiber having the same length and outer diameter as those of the nanotube (see Fig. 9). The latter are adopted to preserve the morphological features of the nanotube as the reinforcing phase. As a result, the elastic properties of the effective fiber will differ from those of the nanotube and need to be determined separately. Under an isostrain condition, the effective Young's modulus of the effective fiber, E^f, can be readily obtained as

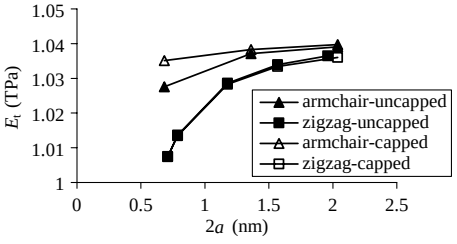

Fig. 8. Young's modulus of nanotubes ($L_t/a = 50$).

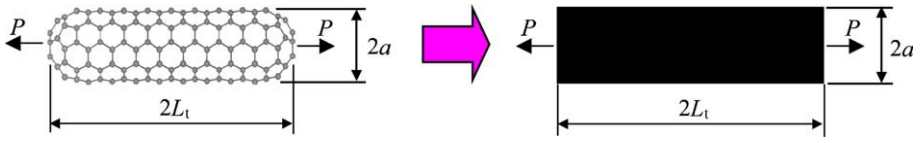

Fig. 9. Nanotube as an effective fiber.

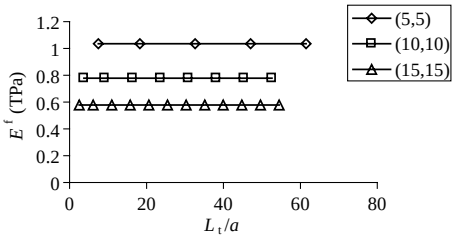

Fig. 10. Young's modulus of effective fibers (armchair).

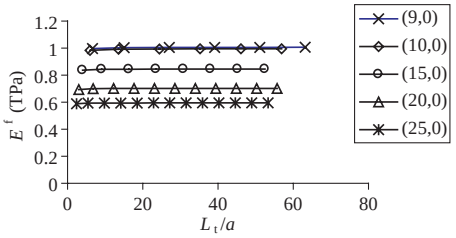

Fig. 11. Young's modulus of effective fibers (zigzag).

Table 1
Diameter and Young's modulus of the effective fiber

Armchair	$2a$ (nm)	E^f (TPa)	Zigzag	$2a$ (nm)	E^f (TPa)
(5,5)	0.6834	1.035	(9, 0)	0.7086	1.006
(10,10)	1.3594	0.779	(10, 0)	0.7866	0.995
(15,15)	2.0370	0.578	(15, 0)	1.1774	0.845
			(20,0)	1.5684	0.702
			(25, 0)	1.9598	0.594

$$E^f = \frac{a^2 - (a-t)^2}{a^2} E_t. \tag{2}$$

In obtaining Eq. (2) use has also been made of the condition that the axial load carried by the effective fiber, P, is the same as that by the nanotube. The isostrain approximation invoked here is consistent with the shear-lag analysis to be presented next. With both the outer radius (a) and the wall thickness (t) of the nanotube involved in Eq. (2) as two independent variables, the hollowness of the nanotube is directly incorporated in the determination of E^f.

The calculated values of E^f as a function of L_t/a are shown in Figs. 10 and 11. Both figures clearly indicate that the larger the tube diameter is the lower E^f becomes, while L_t/a has negligible effect on E^f. For convenience of later reference, the values of E^f for the different nanotubes considered are also listed in Table 1.

3. Shear-lag model for the nanocomposite

The classical shear-lag model originated by Cox (1952) was later elucidated by McCartney (1992) and Nairn (1997) in the context of linear elasticity. However, in their concentric cylinder models the fiber

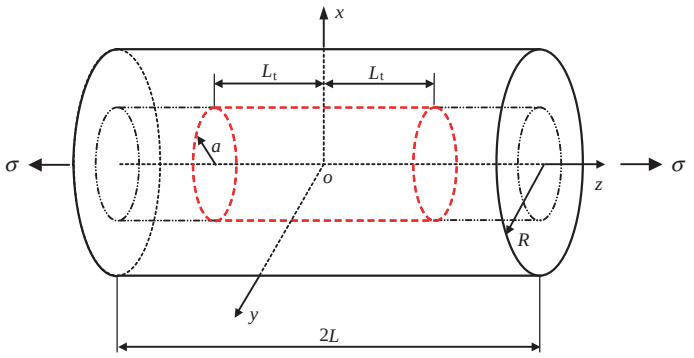

Fig. 12. RVE for the nanocomposite.

and the matrix layer are equally long and the fiber ends are treated as traction-free fiber breaks (cracks). As a result, their models cannot be directly applied to the configuration shown in Fig. 2 or Fig. 12. This necessitates the current shear-lag formulation using the theory of elasticity. Since the purpose of the shear-lag analysis is to describe the mechanisms of load transfer across the entire nanotube–matrix interface, which can be viewed as a global response, the use of continuum mechanics (elasticity) should lead to fairly accurate simulations (Liu and Chen, 2003). In fact, several elasticity-based models have been shown to be capable of accurately predicting the global properties of nanostructured materials (e.g., Lourie et al., 1998; Govindjee and Sackman, 1999; Ru, 2000; Harik, 2001, 2002; Lilleodden et al., 2003).

The derivations presented here are built upon the earlier works of McCartney (1992) and Nairn (1997), and, therefore, the three major assumptions inherent in a shear-lag analysis, which are also invoked in the current formulation (see Eqs. (12), (19), (22) and (28) below), will not be discussed any further. The formulation is based on the RVE illustrated in Fig. 12, where the effective fiber (continuum) has replaced the capped nanotube (discrete) (see Figs. 2 and 9).

The governing equations for the axisymmetric problem, in a displacement formulation and in terms of the polar coordinates (r, θ, z), include the equilibrium equations (in the absence of body forces):

$$\frac{\partial \sigma_{rr}}{\partial r} + \frac{\partial \tau_{rz}}{\partial z} + \frac{\sigma_{rr} - \sigma_{\theta\theta}}{r} = 0, \quad \frac{\partial \tau_{rz}}{\partial r} + \frac{\partial \sigma_{zz}}{\partial z} + \frac{\tau_{rz}}{r} = 0, \tag{3a,b}$$

the geometrical equations:

$$\varepsilon_{rr} = \frac{\partial u}{\partial r}, \quad \varepsilon_{\theta\theta} = \frac{u}{r}, \quad \varepsilon_{zz} = \frac{\partial w}{\partial z}, \quad \gamma_{rz} = \frac{\partial u}{\partial z} + \frac{\partial w}{\partial r}, \tag{4a–d}$$

and the constitutive equations:

$$\begin{aligned} \varepsilon_{rr} &= \frac{1}{E}[\sigma_{rr} - \nu(\sigma_{\theta\theta} + \sigma_{zz})], \quad \varepsilon_{\theta\theta} = \frac{1}{E}[\sigma_{\theta\theta} - \nu(\sigma_{zz} + \sigma_{rr})], \\ \varepsilon_{zz} &= \frac{1}{E}[\sigma_{zz} - \nu(\sigma_{rr} + \sigma_{\theta\theta})], \quad \gamma_{rz} = \frac{\tau_{rz}}{G}. \end{aligned} \tag{5a–d}$$

In Eqs. (3a,b)–(5a–d), σ_{rr}, $\sigma_{\theta\theta}$, σ_{zz} and τ_{rz} are stress components, ε_{rr}, $\varepsilon_{\theta\theta}$, ε_{zz} and γ_{rz} are strain components, u and w are, respectively, the radial and axial displacement components, and E, ν and G are, respectively, the Young's modulus, Poisson's ratio and shear modulus of the material. These three sets of equations are applicable to both the effective fiber and the matrix.

The boundary conditions for this problem are given by

$$\mathbf{t}^{\mathrm{m}}|_{r=R} = \mathbf{0}, \quad \mathbf{t}^{\mathrm{m}}|_{z=\pm L} = \pm\sigma \boldsymbol{e}_3, \tag{6a,b}$$

and the interfacial traction continuity conditions by

$$\mathbf{t}^{\mathrm{f}}|_{r=a,-L_{\mathrm{t}}\leqslant z\leqslant L_{\mathrm{t}}}=\mathbf{t}^{\mathrm{m}}|_{r=a,-L_{\mathrm{t}}\leqslant z\leqslant L_{\mathrm{t}}},\quad \mathbf{t}^{\mathrm{f}}|_{z=\pm L_{\mathrm{t}},0\leqslant r\leqslant a}=\mathbf{t}^{\mathrm{m}}|_{z=\pm L_{\mathrm{t}},0\leqslant r\leqslant a}, \tag{7a,b}$$

where $\mathbf{t}$ is the traction vector, σ is the axial normal stress uniformly applied on $z=\pm L$, and the superscripts f, m denote, respectively, the effective fiber and the matrix.

The exact solution of the boundary-value problem defined by Eqs. (3a,b)–(7a,b) for the current composite cylinder problem involving the two phases with finite dimensions (see Fig. 12) can hardly be obtained. In fact, no closed-form solution has been derived even for the simpler problem of a finite composite cylinder without the two pure matrix regions using elasticity (Smith and Spencer, 1970; Wu et al., 2000). Hence, an approximate solution of the shear-lag type will be sought here, which satisfies, exactly or on average, the governing equations in the longitudinal direction. The derivation will be done separately for the reinforced region ($-L_{\mathrm{t}}\leqslant z\leqslant L_{\mathrm{t}}$) and the pure matrix regions ($-L\leqslant z\leqslant -L_{\mathrm{t}}$ and $L_{\mathrm{t}}\leqslant z\leqslant L$).

3.1. Solution in the reinforced region ($-L_{\mathrm{t}}\leqslant z\leqslant L_{\mathrm{t}}$)

Note that Eq. (3b), which is the equilibrium equation in the z-direction, can be integrated with respect to r from 0 to a to give, for the effective fiber,

$$\frac{1}{\pi a^2}\int_0^a\frac{\partial\sigma_{zz}^{\mathrm{f}}}{\partial z}(2\pi r)\mathrm{d}r+\frac{1}{\pi a^2}\int_0^a\frac{1}{r}\frac{\partial}{\partial r}\left(r\tau_{rz}^{\mathrm{f}}\right)(2\pi r)\mathrm{d}r=0. \tag{8}$$

The average axial normal stress over the cross-section of the effective fiber can be defined as

$$\overline{\sigma_{zz}^{\mathrm{f}}}(z)\equiv\frac{1}{\pi a^2}\int_0^a\sigma_{zz}^{\mathrm{f}}(r,z)(2\pi r)\mathrm{d}r. \tag{9}$$

Then, Eq. (8) becomes, with the use of Eq. (9),

$$\frac{\mathrm{d}\overline{\sigma_{zz}^{\mathrm{f}}}}{\mathrm{d}z}=-\frac{2}{a}\tau_i, \tag{10}$$

where

$$\tau_i\equiv\tau_{rz}^{\mathrm{f}}|_{r=a} \tag{11}$$

is the interfacial shear stress (on the curved interface $r=a$), which is a function of z.

To determine τ_{rz}^{f} using the interfacial shear stress τ_i, assume that

$$\frac{\partial\sigma_{zz}^{\mathrm{f}}}{\partial z}=f(z), \tag{12}$$

where $f(z)$ is a function yet to be determined. Then, using Eq. (12) in Eq. (3b) and integrating with respect to r from 0 to r will lead to

$$\tau_{rz}^{\mathrm{f}}=-\frac{1}{2}rf(z), \tag{13}$$

where use has been made of the fact that both τ_{rz}^{f} and $f(z)$ are finite at $r=0$. By applying Eq. (11) to Eq. (13), $f(z)$ and thus τ_{rz}^{f} will then be determined as

$$f(z)=-\frac{2}{a}\tau_i(z),\quad \tau_{rz}^{\mathrm{f}}=\frac{r}{a}\tau_i. \tag{14a,b}$$

In component form, Eq. (6a) becomes

$$\sigma_{rr}^{\mathrm{m}}|_{r=R}=0,\quad \tau_{zr}^{\mathrm{m}}|_{r=R}=0, \tag{15a,b}$$

and Eq. (7a) reads

$$\sigma_{rr}^{\mathrm{f}}|_{r=a,-L_{\mathrm{t}}\leqslant z\leqslant L_{\mathrm{t}}}=\sigma_{rr}^{\mathrm{m}}|_{r=a,-L_{\mathrm{t}}\leqslant z\leqslant L_{\mathrm{t}}},\quad \tau_{zr}^{\mathrm{f}}|_{r=a,-L_{\mathrm{t}}\leqslant z\leqslant L_{\mathrm{t}}}=\tau_{zr}^{\mathrm{m}}|_{r=a,-L_{\mathrm{t}}\leqslant z\leqslant L_{\mathrm{t}}}. \tag{16a,b}$$

Now integrating Eq. (3b) with respect to r from a to R yields for the matrix, with the use of Eqs. (11), (15b) and (16b),

$$\frac{\mathrm{d}\overline{\sigma_{zz}^{\mathrm{m}}}}{\mathrm{d}z}=\frac{2a}{R^2-a^2}\tau_i, \tag{17}$$

where

$$\overline{\sigma_{zz}^{\mathrm{m}}}(z)\equiv\frac{1}{\pi(R^2-a^2)}\int_a^R\sigma_{zz}^{\mathrm{m}}(r,z)(2\pi r)\mathrm{d}r \tag{18}$$

is the average axial normal stress over the cross-section of the matrix layer.

Similar to that for determining τ_{rz}^{f} (see Eq. (12)), it is assumed that

$$\frac{\partial\sigma_{zz}^{\mathrm{m}}}{\partial z}=g(z), \tag{19}$$

where $g(z)$ is a yet-unknown function. Substituting Eq. (19) into Eq. (3b) and integrating with respect to r from r to R will yield, with the help of Eq. (15b),

$$\tau_{rz}^{\mathrm{m}}=\frac{1}{2}\left(\frac{R^2}{r}-r\right)g(z). \tag{20}$$

It then follows from Eqs. (20), (16b) and (11) that

$$g(z)=\frac{2a}{R^2-a^2}\tau_i(z),\quad \tau_{rz}^{\mathrm{m}}=\frac{a}{R^2-a^2}\left(\frac{R^2}{r}-r\right)\tau_i. \tag{21a,b}$$

Next, assume that for both the effective fiber and matrix,

$$\left|\frac{\partial u}{\partial z}\right|\ll\left|\frac{\partial w}{\partial r}\right|. \tag{22}$$

This leads to, using Eqs. (4d) and (5d),

$$\tau_{rz}^{\mathrm{f}}=G^{\mathrm{f}}\frac{\partial w^{\mathrm{f}}}{\partial r},\quad \tau_{rz}^{\mathrm{m}}=G^{\mathrm{m}}\frac{\partial w^{\mathrm{m}}}{\partial r}. \tag{23a,b}$$

Combining Eqs. (21b) and (23b) and integrating with respect to r from a to R will result in

$$\tau_i(z)=G^{\mathrm{m}}\frac{R^2-a^2}{a}\frac{1}{R^2\ln\frac{R}{a}-\frac{1}{2}(R^2-a^2)}(w_R^{\mathrm{m}}-w_a^{\mathrm{m}}), \tag{24}$$

where

$$w_R^{\mathrm{m}}\equiv w^{\mathrm{m}}|_{r=R},\quad w_a^{\mathrm{m}}\equiv w^{\mathrm{m}}|_{r=a}. \tag{25a,b}$$

Using Eq. (24) in Eq. (21b) then gives

$$\tau_{rz}^{\mathrm{m}}=G^{\mathrm{m}}\frac{(w_R^{\mathrm{m}}-w_a^{\mathrm{m}})}{R^2\ln\frac{R}{a}-\frac{1}{2}(R^2-a^2)}\left(\frac{R^2}{r}-r\right). \tag{26}$$

Substituting Eq. (26) into Eq. (23b) and integrating with respect to r from a to r will lead to

$$w^{\mathrm{m}}(r,z) = w_a^{\mathrm{m}} + \frac{R^2 \ln\frac{r}{a} - \frac{1}{2}(r^2-a^2)}{R^2 \ln\frac{R}{a} - \frac{1}{2}(R^2-a^2)}(w_R^{\mathrm{m}} - w_a^{\mathrm{m}}). \tag{27}$$

To obtain σ_{zz}^{m}, it is further assumed that for both the effective fiber and the matrix,

$$\sigma_{rr} + \sigma_{\theta\theta} \ll \sigma_{zz}. \tag{28}$$

It then follows from Eqs. (4c), (5c) and (28) that

$$\sigma_{zz}^{\mathrm{f}} = E^{\mathrm{f}}\frac{\partial w^{\mathrm{f}}}{\partial z}, \quad \sigma_{zz}^{\mathrm{m}} = E^{\mathrm{m}}\frac{\partial w^{\mathrm{m}}}{\partial z}. \tag{29a,b}$$

Using Eq. (27) in Eq. (29b) gives

$$\sigma_{zz}^{\mathrm{m}} = \sigma_i^{\mathrm{m}} + \frac{R^2 \ln\frac{r}{a} - \frac{1}{2}(r^2-a^2)}{R^2 \ln\frac{R}{a} - \frac{1}{2}(R^2-a^2)}(\sigma_{zz}^{\mathrm{m}}|_{r=R} - \sigma_i^{\mathrm{m}}), \tag{30}$$

where

$$\sigma_i^{\mathrm{m}} \equiv \sigma_{zz}^{\mathrm{m}}|_{r=a} \tag{31}$$

is the axial normal stress on the interface $r = a$. To find $\sigma_{zz}^{\mathrm{m}}|_{r=R}$, consider the force balance of the composite cylinder along the z-direction:

$$\pi R^2 \sigma = \int_0^a \sigma_{zz}^{\mathrm{f}}(2\pi r)\mathrm{d}r + \int_a^R \sigma_{zz}^{\mathrm{m}}(2\pi r)\mathrm{d}r. \tag{32}$$

Using Eqs. (9) and (30) in Eq. (32) and carrying out the algebra will yield

$$\sigma_{zz}^{\mathrm{m}}|_{r=R} = \sigma_i^{\mathrm{m}} + \frac{R^2 \ln\frac{R}{a} - \frac{1}{2}(R^2-a^2)}{R^4 \ln\frac{R}{a} - \frac{1}{4}(R^2-a^2)(3R^2-a^2)}\left[R^2\sigma - a^2\overline{\sigma_{zz}^{\mathrm{f}}} - (R^2-a^2)\sigma_i^{\mathrm{m}}\right]. \tag{33}$$

From Eqs. (10), (24), (29b), (31) and (33) it follows that

$$\frac{\mathrm{d}^2\overline{\sigma_{zz}^{\mathrm{f}}}}{\mathrm{d}z^2} = -\frac{1}{1+v^{\mathrm{m}}}\frac{R^2-a^2}{a^2}\frac{1}{R^4 \ln\frac{R}{a} - \frac{1}{4}(R^2-a^2)(3R^2-a^2)}\left[R^2\sigma - a^2\overline{\sigma_{zz}^{\mathrm{f}}} - (R^2-a^2)\sigma_i^{\mathrm{m}}\right]. \tag{34}$$

Note that perfect bonding implies that

$$\varepsilon_{zz}^{\mathrm{m}}|_{r=a} = \varepsilon_{zz}^{\mathrm{f}}|_{r=a}. \tag{35}$$

This condition would remain the same if it were to be expressed in terms of the axial normal strain in the nanotube because of the isostrain condition invoked earlier in obtaining E^{f} from E_{t} (see Eq. (2)). Using Eqs. (4c), (29a,b) and (31) in Eq. (35) then gives

$$\sigma_{zz}^{\mathrm{f}}|_{r=a} = \frac{E^{\mathrm{f}}}{E^{\mathrm{m}}}\sigma_i^{\mathrm{m}}. \tag{36}$$

Considering that the diameter of the nanotube (and thus of the effective fiber) is very small, it is assumed that $\sigma_{zz}^{\mathrm{f}}(r,z)$ can be represented, with good accuracy, by its average $\overline{\sigma_{zz}^{\mathrm{f}}}(z)$. Then, Eq. (36) becomes

$$\sigma_i^{\mathrm{m}} = \frac{E^{\mathrm{m}}}{E^{\mathrm{f}}}\overline{\sigma_{zz}^{\mathrm{f}}}. \tag{37}$$

Substituting Eq. (37) into Eq. (34) leads to

$$\frac{\mathrm{d}^2\overline{\sigma_{zz}^{\mathrm{f}}}}{\mathrm{d}z^2} - \alpha^2\overline{\sigma_{zz}^{\mathrm{f}}} = -\frac{\alpha^2 R^2}{a^2 + \frac{E^{\mathrm{m}}}{E^{\mathrm{f}}}(R^2-a^2)}\sigma, \tag{38}$$

where

$$\alpha^2 = \frac{1}{1+\nu^{\mathrm{m}}}\frac{R^2-a^2}{a^2}\frac{a^2+\frac{E^{\mathrm{m}}}{E^{\mathrm{f}}}(R^2-a^2)}{R^4\ln\frac{R}{a}-\frac{1}{4}(R^2-a^2)(3R^2-a^2)}. \tag{39}$$

The general solution of Eq. (38) is given by

$$\overline{\sigma_{zz}^{\mathrm{f}}} = c_1 e^{\alpha z} + c_2 e^{-\alpha z} + \frac{R^2}{a^2+\frac{E^{\mathrm{m}}}{E^{\mathrm{f}}}(R^2-a^2)}\sigma, \tag{40}$$

where c_1 and c_2 are two constants to be determined from the boundary conditions.

Using Eq. (40) in Eq. (10) yields

$$\tau_i = -\frac{a}{2}\alpha(c_1 e^{\alpha z} - c_2 e^{-\alpha z}). \tag{41}$$

The substitution of Eqs. (33), (37) and (40) into Eq. (30) leads to

$$\sigma_{zz}^{\mathrm{m}} = \frac{\left[R^2\ln\frac{r}{a}-\frac{1}{2}(r^2-a^2)\right]R^2}{R^4\ln\frac{R}{a}-\frac{1}{4}(R^2-a^2)(3R^2-a^2)}\sigma + \left\{\frac{E^{\mathrm{m}}}{E^{\mathrm{f}}} - \frac{\left[a^2+\frac{E^{\mathrm{m}}}{E^{\mathrm{f}}}(R^2-a^2)\right]\left[R^2\ln\frac{r}{a}-\frac{1}{2}(r^2-a^2)\right]}{R^4\ln\frac{R}{a}-\frac{1}{4}(R^2-a^2)(3R^2-a^2)}\right\} \times \left[c_1 e^{\alpha z} + c_2 e^{-\alpha z} + \frac{R^2}{a^2+\frac{E^{\mathrm{m}}}{E^{\mathrm{f}}}(R^2-a^2)}\sigma\right]. \tag{42}$$

Finally, the use of Eq. (41) in Eq. (14b) gives

$$\tau_{rz}^{\mathrm{f}} = -\frac{\alpha}{2}(c_1 e^{\alpha z} - c_2 e^{-\alpha z})r, \tag{43}$$

and Eq. (41) in Eq. (21b) results in

$$\tau_{rz}^{\mathrm{m}} = -\frac{a^2\alpha}{2(R^2-a^2)}\left(\frac{R^2}{r}-r\right)(c_1 e^{\alpha z} - c_2 e^{-\alpha z}). \tag{44}$$

Clearly, the interfacial shear stress τ_i and the stress components $\overline{\sigma_{zz}^{\mathrm{f}}}(z)$, τ_{rz}^{f}, σ_{zz}^{m} and τ_{rz}^{m} in the effective fiber and the matrix in the reinforced region ($-L_{\mathrm{t}} \leqslant z \leqslant L_{\mathrm{t}}$) will be completely determined from Eqs. (40)–(44) once the constants c_1 and c_2 have been found. The determination of c_1 and c_2 requires the use of the solution in the pure matrix regions.

3.2. Solution in the pure matrix regions ($-L \leqslant z \leqslant -L_{\mathrm{t}}$ and $L_{\mathrm{t}} \leqslant z \leqslant L$)

Each of the two pure matrix cylinders at the ends of the RVE may still be viewed as a composite cylinder reinforced by a virtual fiber having the same diameter as that of the effective fiber (or nanotube) and the same Young's modulus and Poisson's ratio as those of the matrix material. As a result, the solution derived above for the composite region ($-L_{\mathrm{t}} \leqslant z \leqslant L_{\mathrm{t}}$) can be applied to the pure matrix regions ($-L \leqslant z \leqslant -L_{\mathrm{t}}$ and $L_{\mathrm{t}} \leqslant z \leqslant L$) by replacing E^{f} with E^{m}. Hence, from Eq. (40) it follows that, with $E^{\mathrm{f}} = E^{\mathrm{m}}$,

$$\overline{\sigma_{zz}^{\mathrm{fm}}} = c_3 e^{\alpha_{\mathrm{m}} z} + c_4 e^{-\alpha_{\mathrm{m}} z} + \sigma, \tag{45}$$

where the superscript fm refers to the virtual fiber, c_3 and c_4 are two unknown constants, and α_{m} is obtained from Eq. (39), with $E^{\mathrm{f}} = E^{\mathrm{m}}$, as

$$\alpha_{\mathrm{m}}^2 = \frac{1}{1+\nu^{\mathrm{m}}}\frac{R^2-a^2}{a^2}\frac{R^2}{R^4\ln\frac{R}{a}-\frac{1}{4}(R^2-a^2)(3R^2-a^2)}. \tag{46}$$

The use of Eqs. (10) and (45) in Eq. (14b) gives

$$\tau_{rz}^{\mathrm{fm}} = -\frac{r}{2}\alpha_{\mathrm{m}}(c_3 \mathrm{e}^{\alpha_{\mathrm{m}} z} - c_4 \mathrm{e}^{-\alpha_{\mathrm{m}} z}). \tag{47}$$

Note that in component form Eq. (6b) reads

$$\sigma_{zz}^{\mathrm{m}}|_{z=\pm L} = \sigma, \quad \tau_{rz}^{\mathrm{m}}|_{z=\pm L} = 0, \tag{48a, b}$$

and Eq. (7b) becomes

$$\sigma_{zz}^{\mathrm{f}}|_{z=\pm L_{\mathrm{t}}, 0\leqslant r\leqslant a} = \sigma_{zz}^{\mathrm{m}}|_{z=\pm L_{\mathrm{t}}, 0\leqslant r\leqslant a}, \quad \tau_{rz}^{\mathrm{f}}|_{z=\pm L_{\mathrm{t}}, 0\leqslant r\leqslant a} = \tau_{rz}^{\mathrm{m}}|_{z=\pm L_{\mathrm{t}}, 0\leqslant r\leqslant a}. \tag{49a,b}$$

Applying Eq. (48a) to Eq. (45) gives

$$c_3 = c_4 = 0, \tag{50}$$

which leads to, upon its substitution into Eqs. (45) and (47),

$$\overline{\sigma_{zz}^{\mathrm{fm}}} = \sigma, \quad \tau_{rz}^{\mathrm{fm}} = 0. \tag{51a,b}$$

Clearly, Eq. (48b) is satisfied by the shear stress component given in Eq. (51b).

Next, using Eqs. (40) and (51a) in Eq. (49a) yields

$$c_1 = c_2 = \frac{\sigma}{2\cosh(\alpha L_{\mathrm{t}})}\left[1 - \frac{R^2}{a^2 + \frac{E^{\mathrm{m}}}{E^{\mathrm{f}}}(R^2 - a^2)}\right]. \tag{52}$$

The substitution of Eq. (52) into Eqs. (40)–(44) will then lead to the stress components in the reinforced region ($-L_{\mathrm{t}} \leqslant z \leqslant L_{\mathrm{t}}$). The results give

$$\overline{\sigma_{zz}^{\mathrm{f}}} = \left\{\frac{R^2}{a^2 + \frac{E^{\mathrm{m}}}{E^{\mathrm{f}}}(R^2 - a^2)} + \left[1 - \frac{R^2}{a^2 + \frac{E^{\mathrm{m}}}{E^{\mathrm{f}}}(R^2 - a^2)}\right]\frac{\cosh(\alpha z)}{\cosh(\alpha L_{\mathrm{t}})}\right\}\sigma, \tag{53a}$$

$$\tau_i = \frac{a\alpha\sinh(\alpha z)}{2\cosh(\alpha L_{\mathrm{t}})}\frac{(R^2 - a^2)\left(1 - \frac{E^{\mathrm{m}}}{E^{\mathrm{f}}}\right)}{a^2 + \frac{E^{\mathrm{m}}}{E^{\mathrm{f}}}(R^2 - a^2)}\sigma, \tag{53b}$$

$$\tau_{rz}^{\mathrm{f}} = \frac{r\alpha\sinh(\alpha z)}{2\cosh(\alpha L_{\mathrm{t}})}\frac{(R^2 - a^2)\left(1 - \frac{E^{\mathrm{m}}}{E^{\mathrm{f}}}\right)}{a^2 + \frac{E^{\mathrm{m}}}{E^{\mathrm{f}}}(R^2 - a^2)}\sigma, \tag{53c}$$

$$\sigma_{zz}^{\mathrm{m}} = \frac{\left[R^2\ln\frac{r}{a} - \frac{1}{2}(r^2 - a^2)\right]R^2}{R^4\ln\frac{R}{a} - \frac{1}{4}(R^2 - a^2)(3R^2 - a^2)}\sigma + \left\{\frac{E^{\mathrm{m}}}{E^{\mathrm{f}}} - \frac{\left[a^2 + \frac{E^{\mathrm{m}}}{E^{\mathrm{f}}}(R^2 - a^2)\right]\left[R^2\ln\frac{r}{a} - \frac{1}{2}(r^2 - a^2)\right]}{R^4\ln\frac{R}{a} - \frac{1}{4}(R^2 - a^2)(3R^2 - a^2)}\right\}$$
$$\times\left\{\frac{R^2}{a^2 + \frac{E^{\mathrm{m}}}{E^{\mathrm{f}}}(R^2 - a^2)} + \left[1 - \frac{R^2}{a^2 + \frac{E^{\mathrm{m}}}{E^{\mathrm{f}}}(R^2 - a^2)}\right]\frac{\cosh(\alpha z)}{\cosh(\alpha L_{\mathrm{t}})}\right\}\sigma, \tag{53d}$$

$$\tau_{rz}^{\mathrm{m}} = \frac{\alpha\sinh(\alpha z)}{2\cosh(\alpha L_{\mathrm{t}})}\frac{a^2\left(1 - \frac{E^{\mathrm{m}}}{E^{\mathrm{f}}}\right)}{a^2 + \frac{E^{\mathrm{m}}}{E^{\mathrm{f}}}(R^2 - a^2)}\left(\frac{R^2}{r} - r\right)\sigma, \tag{53e}$$

where the hollowness of the nanotube is accounted for through E^{f} (see Eq. (2)). The stress components in the two pure matrix regions can then be readily obtained from Eqs. (53a–e) by letting $E^{\mathrm{f}} = E^{\mathrm{m}}$. The results give

$$\overline{\sigma_{zz}^{\mathrm{fm}}} = \sigma_{zz}^{\mathrm{m}} = \sigma, \quad \tau_{rz}^{\mathrm{fm}} = \tau_i = \tau_{rz}^{\mathrm{m}} = 0, \tag{54a,b}$$

which represent a homogeneous deformation induced by the uniform uniaxial tension, as expected.

4. Numerical results

To illustrate the shear-lag model developed in the preceding section, parametric studies are conducted for nanotube-reinforced polymer composites using the newly derived formulas. Sample numerical results are presented below.

Fig. 13 shows how the normalized interfacial shear stress and average axial normal stress in the nanotube vary along the nanotube length for three cases having different nanotube aspect ratios (ARs). To compare with the corresponding results of Li and Chou (2003b), values of the controlling parameters for the composite under consideration are taken to be the same as those used in Li and Chou (2003b), i.e., $E^{\mathrm{m}} = 2.41$ GPa, $\nu^{\mathrm{m}} = 0.35$, $E^{\mathrm{f}} = 1000$ GPa, $a = 0.471$ nm, and $R = 5a$. The first two matrix material properties are typical for an epoxy polymer. A comparison shows that in all of the three cases (with different aspect ratios) considered the trends of both τ_i/σ and $\overline{\sigma_{zz}^{\mathrm{f}}}/\sigma$ varying with $z/(2a)$, as predicted by the current shear-lag model, are the same as those predicted by the computational model of Li and Chou (2003b). Moreover, the magnitudes of both τ_i/σ and $\overline{\sigma_{zz}^{\mathrm{f}}}/\sigma$ predicted respectively by the two different models are not too far apart, which can be difficult to achieve in continuum-based simulations of nanostructured materials (e.g., Liu and Chen, 2003). These agreements verify the feasibility of the current model.

To further demonstrate applications of the new model, a second nanocomposite is considered. At this time the properties of the polymer matrix are taken to be the same as those used above (i.e., $E^{\mathrm{m}} = 2.41$ GPa, $\nu^{\mathrm{m}} = 0.35$), but the Young's modulus of the effective fiber is now $E^{\mathrm{f}} = 1006$ GPa, which represents the (9,0) zigzag nanotube with the outer diameter $2a = 0.7086$ nm, as listed in Table 1. Again, $R = 5a$ and the same three aspect ratios are used in the current simulation. The results are illustrated in Figs. 14–17.

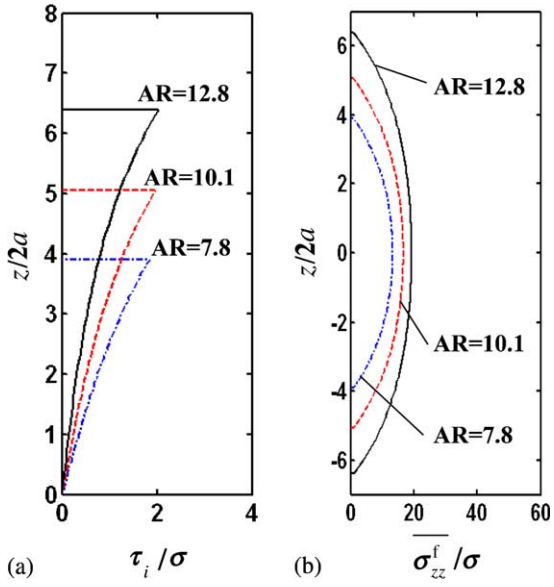

Fig. 13. Interfacial shear stress (a) and average axial normal stress in the nanotube (b).

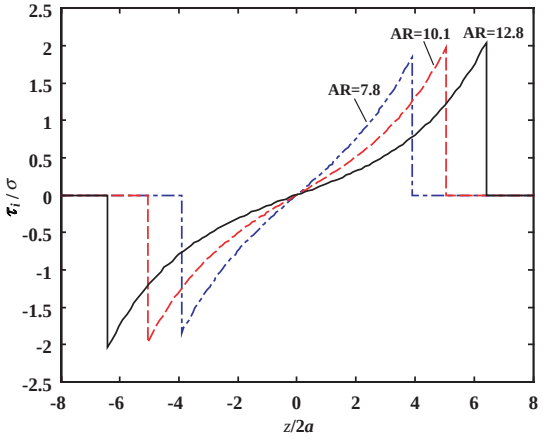

Fig. 14. Interfacial shear stress.

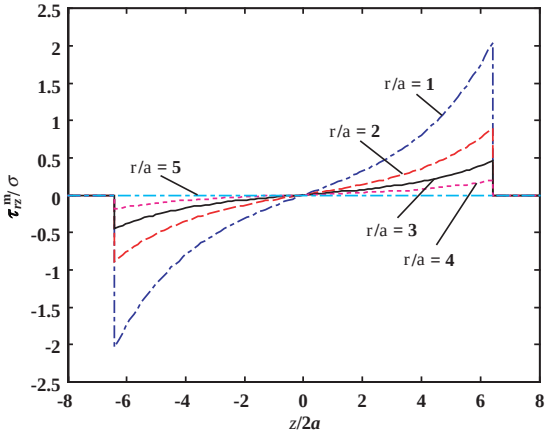

Fig. 15. Shear stress in the matrix (with AR = 12.8).

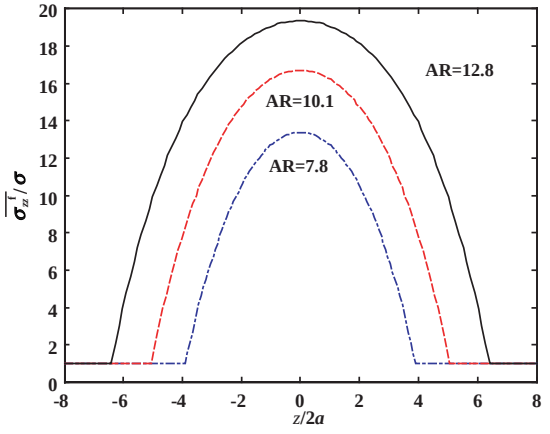

Fig. 16. Average axial normal stress in the nanotube.

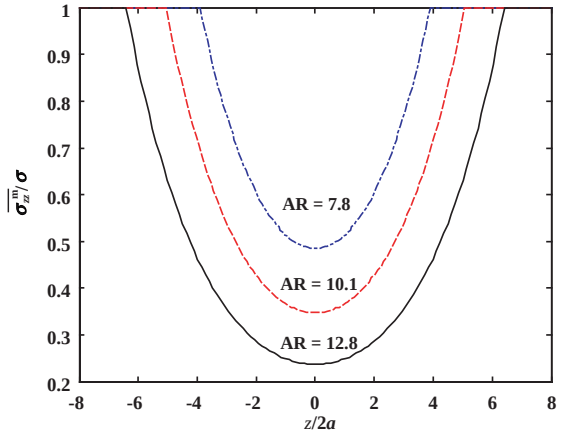

Fig. 17. Average axial normal stress in the matrix.

The variation of the interfacial shear stress along the nanotube length is illustrated in Fig. 14, while that of the shear stress in the matrix in Fig. 15. From Fig. 14 it is seen that the maximum shear stress transfer occurs near the two ends of the nanotube, but the middle of the nanotube is shear stress free due to symmetry. Also, the larger the aspect ratio is, the smaller the interfacial shear stress (at the same z and for given a and σ) becomes. These agree with those observed in Li and Chou (2003b). Fig. 15 shows that the same is true for the shear stress distribution in the matrix: the maximum of the shear stress occurring at the ends and the minimum (zero-valued) in the center of the reinforcing length (i.e., at $z = 0$). In addition, it is observed from Fig. 15 that the shear stress τ_{rz}^{m} decreases rapidly with the increase of the radial distance from the nanotube–matrix interface and that the traction-free boundary condition on the outer surface of the matrix layer (i.e., $r/a = 5 \equiv R/a$) is exactly satisfied, as expected.

Fig. 16 shows the distribution of the average axial normal stress in the nanotube along the nanotube length, while Fig. 17 illustrates that of the average axial normal stress in the matrix. Clearly, it is observed from Fig. 16 that the maximum axial normal stress is reached in the middle of the nanotube, whereas the minimum occurs at its two ends. Also, it is seen that the larger the aspect ratio, the higher the average axial normal stress at the same z for given a and σ. The opposite trends are seen for the average normal stress in the matrix, as shown in Fig. 17. In fact, this is dictated by the global equilibrium requirement. More importantly, it can be noticed from comparing Figs. 16 and 17 that when the nanotube aspect ratio is sufficiently large, most of the applied load in the axial direction can be taken up by the nanotube and the surrounding matrix needs to support only a small portion of the axial loading. For example, when AR = 12.8 the portion of the applied load taken by the nanotube on the cross-section $z = 0$ is more than three times as large as that by the matrix on the same cross-section, although the cross-sectional area of the matrix is twenty-four times as big as that of the effective fiber on $z = 0$ in the current RVE with $R = 5a$. However, this is no longer the case if the nanotube aspect ratio becomes small. For instance, when AR = 7.8 both of the nanotube and the matrix on the cross-section $z = 0$ take about the equal amount of the applied load. These reveal that the nanotube aspect ratio is a critical controlling parameter for nanotube-reinforced composites, and that for significant reinforcements nanotubes with large aspect ratios should be used. This observation conforms to what has been found in existing experimental and computational studies (e.g., Qian et al., 2000; Frankland et al., 2003), thereby further supporting the newly developed analytical model.

5. Summary

A shear-lag model for predicting the interfacial stress transfer in carbon nanotube-reinforced polymer composites is developed using a multiscale approach. A concentric composite cylinder embedded with a capped nanotube is utilized as a representative volume element (RVE) to capture the major morphological features of the nanocomposites. The atomistic structure of the capped nanotube is incorporated in the model by using the molecular structural mechanics of Li and Chou (2003a), which leads to the determination of the effective Young's modulus of the nanotube. The capped nanotube is equivalently replaced by an effective (solid) fiber having the same diameter and length, whose elastic modulus is determined from that of the nanotube under an isostrain condition. The continuum-based shear-lag analysis is carried out using the elasticity theory for axisymmetric problems, which results in closed-form formulas for calculating the interfacial shear stress and other axial stress components in both the nanotube and the matrix.

The formulas are directly applied to sample cases to demonstrate the newly developed model. The numerical results show that the predictions by the current analytical model are in qualitative agreement with those by the computational model of Li and Chou (2003b). The numerical data also reveal that the nanotube aspect ratio plays a critical role in designing the nanotube-reinforced polymer composites, and that the nanotubes with sufficiently large aspect ratios should be used to achieve better reinforcements. These agree with the findings from earlier experimental and computational studies.

Finally, it should be mentioned that replacing the capped nanotube (discrete) by an effective fiber with square ends (continuum) is to make the problem analytically tractable in the context of elasticity. The effect of the caps on Young's modulus of the capped nanotube (E_t) is incorporated in Eq. (1) through the parameter β. This effect is subsequently included in the determination of the modulus of the effective fiber (E^f) using Eq. (2) and then in the computation of the stress components using Eqs. (53a–e). However, the use of square ends (rather than hemispherical ones) does lead to over-predicted stress concentrations near the two ends of the nanotube, as was also observed by Li and Chou (2003b). This remains to be a major limitation of the new model. Nevertheless, the predicted stress distributions far away from the two tube ends should be fairly accurate, since typical nanotubes tend to have very large aspect ratios and the end effects are localized. In fact, it has been observed in the present study that the effect of capping on the elastic modulus of the nanotube is insignificant for sufficiently long and large nanotubes (see Fig. 8). Moreover, the current analysis, as an upper-bound estimate, would lead to conservative designs of nanotube-reinforced polymer composites.

Acknowledgments

The work reported here is partially funded by a grant from the US AFOSR (Grant # F49620-03-1-0442, with Dr. B.-L. Lee as the Program Manager). This support is gratefully acknowledged. The authors also wish to thank Dr. A.K. Roy of the US AFRL/MLBC for supporting the project. In addition, the authors are indebted to two anonymous reviewers for their helpful comments on an earlier version of this paper.

References

Ajayan, P.M., Schadler, L.S., Giannaris, C., Rubio, A., 2000. Single-walled carbon nanotube–polymer composites: strength and weakness. Adv. Mater. 12, 750–753.

Barber, A.H., Cohen, S.R., Wagner, H.D., 2003. Measurement of carbon nanotube–polymer interfacial strength. Appl. Phys. Lett. 82, 4140–4142.

Bower, C., Zhu, W., Jin, S., Zhou, O., 2000. Plasma-induced alignment of carbon nanotubes. Appl. Phys. Lett. 77, 830–832.

Chang, T., Gao, H., 2003. Size-dependent elastic properties of a single-walled carbon nanotube via a molecular mechanics model. J. Mech. Phys. Solids 51, 1059–1074.

Cooper, C.A., Ravich, D., Lips, D., Mayer, J., Wagner, H.D., 2002. Distribution and alignment of carbon nanotubes and nanofibrils in a polymer matrix. Compos. Sci. Technol. 62, 1105–1112.

Cox, H.L., 1952. The elasticity and strength of paper and other fibrous materials. Brit. J. Appl. Phys. 3, 72–79.

Frankland, S.J.V., Harik, V.M., 2003. Analysis of carbon nanotube pull-out from a polymer matrix. Surf. Sci. 525, L103–L108.

Frankland, S.J.V., Caglar, A., Brenner, D.W., Griebel, M., 2002. Molecular simulation of the influence of chemical cross-links on the shear strength of carbon nanotube-polymer interfaces. J. Phys. Chem. B 106, 3046–3048.

Frankland, S.J.V., Harik, V.M., Odegard, G.M., Brenner, D.W., Gates, T.S., 2003. The stress–strain behavior of polymer–nanotube composites from molecular dynamics simulation. Compos. Sci. Technol. 63, 1655–1661.

Fujita, M., Saito, R., Dresselhaus, G., Dresselhaus, M.S., 1992. Formation of general fullerenes by their projection on a honeycomb lattice. Phys. Rev. B 45, 13834–13836.

Gao, X.-L., Li, K., 2003. Finite deformation continuum model for single-walled carbon nanotubes. Int. J. Solids Struct. 40, 7329–7337.

Glukhova, O.E., Zhbanov, A.I., Torgashov, I.G., Sinitsyn, N.I., Torgashov, G.V., 2003. Ponderomotive forces effect on the filed emission of carbon nanotube films. Appl. Surf. Sci. 215, 149–159.

Govindjee, S., Sackman, J.L., 1999. On the use of continuum mechanics to estimate the properties of nanotubes. Solid State Commun. 110, 227–230.

Haggenmueller, R., Gommans, H.H., Rinzler, A.G., Fischer, J.E., Winey, K.I., 2000. Aligned single-wall carbon nanotubes in composites by melt processing methods. Chem. Phys. Lett. 330, 219–225.

Harik, V.M., 2001. Ranges of applicability for the continuum beam model in the mechanics of carbon nanotubes and nanorods. Solid State Commun. 120, 331–335.

Harik, V.M., 2002. Mechanics of carbon nanotubes: applicability of the continuum-beam models. Comput. Mater. Sci. 24, 328–342.

Harris, P.J.F., 1999. Carbon Nanotubes and Related Structures. Cambridge University Press, Cambridge.

Li, C., Chou, T.-W., 2003a. A structural mechanics approach for the analysis of carbon nanotubes. Int. J. Solids Struct. 40, 2487–2499.

Li, C., Chou, T.-W., 2003b. Multiscale modeling of carbon nanotube reinforced polymer composites. J. Nanosci. Nanotech. 3, 1–8.

Li, K., Gao, X.-L., Roy, A.K., 2003. Micromechanical analysis of three-dimensional open-cell foams using the matrix method for space frame structures. In: Proceedings of the 14th International Conference on Composite Materials (ICCM-14), San Diego, CA, July 14–18, 2003.

Liao, K., Li, S., 2001. Interfacial characteristics of a carbon nanotube–polystyrene composite system. Appl. Phys. Lett. 79, 4225–4227.

Lilleodden, E.T., Zimmerman, J.A., Foiles, S.M., Nix, W.D., 2003. Atomistic simulations of elastic deformation and dislocation nucleation during nanoindentation. J. Mech. Phys. Solids 51, 901–920.

Liu, Y.J., Chen, X.L., 2003. Continuum models of carbon nanotube-based composites using the boundary element method. Electron. J. Bound. Elem. 1, 316–335.

Lordi, V., Yao, N., 2000. Molecular mechanics of binding in carbon-nanotube–polymer composites. J. Mater. Res. 15, 2770–2779.

Lourie, O., Cox, D.M., Wagner, H.D., 1998. Buckling and collapse of embedded carbon nanotubes. Phys. Rev. Lett. 81, 1638–1641.

Maruyama, B., Alam, K., 2002. Carbon nanotubes and nanofibers in composite materials. SAMPE J. 38 (3), 59–68.

McCartney, L.N., 1992. Analytical models of stress transfer in unidirectional composites and cross-ply laminates, and their application to the prediction of matrix/transverse cracking. In: Reddy, J.N., Reifsnider, K.L. (Eds.), Local Mechanics Concepts for Composite Material Systems, Proceedings of IUTAM Symposium, Blacksburg, VA, October 28–31, 1991. Springer-Verlag, Berlin, pp. 251–282.

Nairn, J.A., 1997. On the use of shear-lag methods for analysis of stress transfer in unidirectional composites. Mech. Mater. 26, 63–80.

Odegard, G.M., Gates, T.S., Nicholson, L.M., Wise, K.E., 2002. Equivalent-continuum modeling of nano-structured materials. Compos. Sci. Technol. 62, 1869–1880.

Pantano, A., Parks, D.M., Boyce, M.C., 2004. Mechanics of deformation of single- and multi-wall carbon nanotubes. J. Mech. Phys. Solids 52, 789–821.

Popov, V.N., Van Doren, V.E., Balkanski, M., 2000. Elastic properties of single-walled carbon nanotubes. Phys. Rev. B 61, 3078–3084.

Qian, D., Dickey, E.C., Andrews, R., Rantell, T., 2000. Load transfer and deformation mechanisms in carbon nanotube–polystyrene composites. Appl. Phys. Lett. 76, 2868–2870.

Ru, C.Q., 2000. Effective bending stiffness of carbon nanotubes. Phy. Rev. B 62, 9973–9976.

Saito, R., Fujita, M., Dresselhaus, G., Dresselhaus, M.S., 1992. Electronic structure of chiral graphene tubules. Appl. Phys. Lett. 60, 2204–2206.

Saito, R., Fujita, M., Dresselhaus, G., Dresselhaus, M.S., 1993. Electronic structure and growth mechanism of carbon tubules. Mater. Sci. Eng. B 19, 185–191.

Schadler, L.S., Giannaris, S.C., Ajayan, P.M., 1998. Load transfer in carbon nanotube epoxy composites. Appl. Phys. Lett. 73, 3842–3844.

Smith, G.E., Spencer, A.J.M., 1970. Interfacial tractions in a fibre-reinforced elastic composite material. J. Mech. Phys. Solids 18, 81–100.

Thostenson, E.T., Chou, T.-W., 2002. Aligned multi-walled carbon nanotube-reinforced composites: processing and mechanical characterization. J. Phys. D: Appl. Phys. 35, L77–L80.

Thostenson, E.T., Chou, T.-W., 2003. On the elastic properties of carbon nanotube-based composites: modeling and characterization. J. Phys. D: Appl. Phys. 36, 573–582.

Thostenson, E.T., Ren, Z., Chou, T.-W., 2001. Advances in the science and technology of carbon nanotubes and their composites: a review. Compos. Sci. Technol. 61, 1899–1912.

Wagner, H.D., 2002. Nanotube–polymer adhesion: a mechanics approach. Chem. Phys. Lett. 361, 57–61.

Wagner, H.D., Lourie, O., Feldman, Y., Tenne, R., 1998. Stress-induced fragmentation of multiwall carbon nanotubes in a polymer matrix. Appl. Phys. Lett. 72, 188–190.

Wu, Z.J., Ye, J.Q., Cabrera, J.G., 2000. 3D analysis of stress transfer in the micromechanics of fiber reinforced composites by using an eigen-function expansion method. J. Mech. Phys. Solids 48, 1037–1063.

Yao, N., Lordi, V., 1998. Carbon nanotube caps as springs: molecular dynamics simulations. Phys. Rev. B 58, 12649–12651.

Zhang, P., Huang, Y., Geubelle, P.H., Klein, P.A., Hwang, K.C., 2002. The elastic modulus of single-wall carbon nanotubes: a continuum analysis incorporating interatomic potentials. Int. J. Solids Struct. 39, 3893–3906.